Journal of Energy Chemistry 104 (2025) 136–145

Contents lists available at ScienceDirect

Journal of Energy Chemistry

journal homepage: www.elsevier.com/locate/jechem

http://www.journals.elsevier.com/journal-of-energy-chemistry/

Complementary self-assembled monolayers enabling improved energy level alignment in inverted perovskite solar cells

Shantao Zhang [a,1], Xiaofen Jiang [a,b,1], Xue Wang [a,1], Yan Gao [a,1], TianAo Hou [a], Xiaoqian Teng [a], Haolin Wang [a], Wenjing Chen [c], Shuang Gao [a], Xinyu Li [a], Ziqi Hu [a,*], Xiaojun Wu [a], Zhengguo Xiao [c], Tao Chen [a], Yanwu Zhu [a], Yalin Lu [a], Xiaocheng Zeng [d], Zonglong Zhu [b,*], Shangfeng Yang [a,*]

[a] Key Laboratory of Precision and Intelligent Chemistry, Collaborative Innovation Center of Chemistry for Energy Materials (iChEM), Department of Materials Science and Engineering, University of Science and Technology of China, Hefei 230026, Anhui, China
[b] Department of Chemistry, and Shenzhen Research Institute, City University of Hong Kong, Kowloon, Hong Kong 999077, China
[c] Department of Physics, CAS Key Laboratory of Strongly-Coupled Quantum Matter Physics, University of Science and Technology of China, Hefei 230026, Anhui, China
[d] Department of Materials Science and Engineering, City University of Hong Kong, Kowloon, Hong Kong 999077, China

ARTICLE INFO

Article history:
Received 26 October 2024
Revised 15 December 2024
Accepted 19 December 2024
Available online 6 January 2025

Keywords:
Perovskite solar cells
Self-assembled monolayer
Hole-selective layer
Dibenzo[c,g]carbazole
Dipole moment

ABSTRACT

Self-assembled monolayers (SAMs) have been commonly employed as hole-selective layers (HSLs) in inverted (p-i-n) perovskite solar cells (PSCs), and typically only a single-component SAM is applied, which plays limited role in selective hole transport. Herein, we synthesize a novel SAM, (4-(3,11-dibromo-7H-dibenzo[c,g]carbazol-7-yl)butyl)phosphonic acid (Br-4PADBC), and apply it as a complementary component to the commonly used [2-(3,6-dimeth oxy-9H-carbazol-9-yl)ethyl]phosphonic acid (MeO-2PACz) SAM, accomplishing boosted hole transport in inverted PSCs. A series of characterizations and theoretical calculations are employed to unravel the roles of each components within the binary SAM (bi-SAM). The involvements of the non-planar dibenzo[c,g]carbazole unit and electron-withdrawing Br atoms induce larger dipole moment of Br-4PADBC than MeO-2PACz, resulting in much deeper work function of ITO and consequently improved alignment with the valence band energy level of perovskite. Besides, the introduced Br atoms improve the quality of perovskite crystals and help passivate defects of perovskite. On the other hand, the existence of the conventional MeO-2PACz SAM ensures the considerable conductivity of the bi-SAM and thus efficient hole extraction from the perovskite layer. As a result, inverted PSC devices based on bi-SAM HSL deliver a decent power conversion efficiency (PCE) of 24.52% as well as dramatically improved thermal and operational stabilities.

1. Introduction

Organic-inorganic hybrid perovskite solar cells (PSCs) have achieved tremendous advancements during the past decade, and are regarded as the most promising next-generation photovoltaic technology [1–6]. Among the state-of-the-art PSCs, inverted (p-i-n) PSCs have garnered considerable attention in recent years due to their processibility at low temperatures, exceptional stability, and suitability for flexible and tandem devices [7–10]. For p-i-n PSC devices, hole-selective layers (HSLs) capable of selectively transporting holes from perovskite layer to anode play a critical role in realizing efficient and stable device [11,12]. In particular, self-assembled monolayers (SAMs) featuring considerable hole selectivity, work function regulation, and passivation of perovskite defects have been commonly used as HSLs in inverted PSCs, contributing to high power conversion efficiency (PCE) exceeding 25% [13–17]. Generally, SAM molecule consists of the anchoring, the spacer, and the terminal groups, and exhibits dipole moment due to the difference in the chemical structures of these three parts [11,18]. Among them, the terminal groups can greatly regulate not only the work function of the bottom substrate but also the morphology and crystallinity of the atop perovskite layer [19]. Noteworthy, for most of the reported high-efficiency inverted PSCs, typically only a single-component SAM is applied, which plays limited role in selective hole transport [20–22]. For instance, for the

* Corresponding authors.
E-mail addresses: huziqi@ustc.edu.cn (Z. Hu), zonglzhu@cityu.edu.hk (Z. Zhu), sfyang@ustc.edu.cn (S. Yang).
[1] These authors contributed equally to this work.

https://doi.org/10.1016/j.jechem.2024.12.040

commonly used [2-(3,6-dimethoxy-9H-carbazol-9-yl)ethyl]phosphonic acid (MeO-2PACz) SAM, the presence of the electron-donating dimethoxy (MeO) groups grafted on the carbazole terminal group results in a small dipole moment of 0.2 D, hindering effective modification of the work function of the bottom indium tin oxide (ITO) [14]. Consequently, an energy level mismatch between ITO and perovskite exists, resulting in inferior open-circuit voltage (V_{OC}) of the PSC device. Moreover, the planar carbazole terminal group of SAMs causes facile π-π stacking and aggregations of multiple SAM molecules in solution, resulting in the formation of defects during SAM growth, which in turn induces the recombination of charge carriers at the perovskite/HSL interface [23]. Hence, designing novel SAMs bearing non-planar terminal group and large dipole moment is highly desired.

Incorporating an additional component into SAM to form a binary SAM (abbreviated bi-SAM) with complementary functionalities has been proposed very recently to improve effectively the HSL performance of inverted PSC devices [17,24–30]. For instance, Tan et al. mixed two homologous SAM molecules, 2PACz ([2-(9H-carbazol9-yl)ethyl]phosphonic acid) and MeO-2PACz, and deposited the bi-SAM layer onto NiO nanocrystal film to construct a composite HSL of the flexible wide-bandgap (WBG) inverted PSCs, achieving a high certified efficiency of 24.4% for a flexible all-perovskite tandem solar cell [26]. More recently, Sargent et al. applied a bi-SAM strategy through incorporating 3-mercaptopropionic acid (3-MPA) into the 2PACz SAM, and found that the incorporated 3-MPA facilitated the decomposition of higher-order clusters and thereby rendered a more uniform molecular distribution of SAMs [28]. Likewise, Yan et al. introduced phosphocholine chloride (PC) into [4-(3,6-dimethyl-9H-carbazol-9yl)butyl]phosphonic acid (Me-4PACz) SAM, resulting in the enhanced monolayer coverage on NiO_x layer, reduced leakage current, and promoted growth of perovskite crystals [17]. Despite of the positive effect of bi-SAM strategy in performance enhancement of inverted PSC devices reported in these reports, the second component incorporated into the carbazole-based SAM is limited to either homologous simpler-structure SAM or highly polar short-chain molecules. None of these reports utilizes a non-planar terminal group as the second component of bi-SAM.

Herein, by involving a non-planar dibenzo[c,g]carbazole (DBC) unit as the core of the terminal group, we synthesize a novel SAM molecule named (4-(3,11-dibromo-7H-dibenzo[c,g]carbazol-7-yl)butyl)phosphonic acid (Br-4PADBC), and apply it as a second component to the MeO-2PACz SAM, accomplishing complementary hole transport in inverted PSCs. The roles of the individual Br-4PADBC and MeO-2PACz components within the bi-SAM are investigated systematically. The non-planar 3,11-dibromo-7H-dibenzo[c,g]carbazole (Br-DBC) terminal group induces a larger dipole moment of Br-4PADBC than MeO-2PACz and consequently much deeper work function of ITO with better alignment with the valence band energy level of perovskite, and additionally the introduced Br atoms benefit the improved crystallization of perovskite film. Besides, the conventional MeO-2PACz SAM ensures the considerable conductivity of the bi-SAM and fulfills efficient hole extraction from the perovskite layer. Owing to the complementary roles of Br-4PADBC and MeO-2PACz SAMs, the inverted PSC devices based on bi-SAM HSL deliver a much higher PCE of 24.52% than those based on the MeO-2PACz single-SAM (23.91%) as well as higher thermal and operational stabilities.

2. Results and discussion

The novel SAM molecule Br-4PADBC was synthesized via the synthetic route illustrated in Scheme 1. Our motivation is to substitute the planar carbazole terminal group with the non-planar dibenzo[c,g]carbazole (DBC) group so as to regulate the work function of the underneath ITO substrate as well as the interfacial interactions between SAM and perovskite [14,31]. In addition, two Br atoms are grafted at the terminal sites far away from the phosphonic acid anchoring group aiming to reinforce the interfacial contact of SAM with halide perovskite and consequently promote the crystallization of the atop perovskite film [32,33]. Simultaneously, the incorporation of electron-withdrawing Br atoms can enlarge the molecular dipole moment. The synthetic details are given in the Supporting Information. In brief, 6-bromo-2-naphthol was used as the raw material to prepare 3,11-dibromo-7H dibenzo[c,g]carbazole (Br-DBC) through hydrothermal reaction and cyclization reactions. In the next step, Br-DBC reacted with 1,4-dibromobutane via nucleophilic substitution reaction and Michaelis-Arbuzov reaction to produce intermediates, followed by hydrolysis using bromotrimethylsilane, methanol, and water, affording the final product Br-4PADBC.

The chemical structure of Br-4PADBC was characterized by a series of spectroscopies including ^{1}H, ^{13}C, and ^{31}P nuclear magnetic resonance (NMR) spectroscopies as well as time of flight mass spectrometer (TOF-MS) (Figs. S1–S10). According to the ^{1}H NMR spectrum of Br-4PADBC, the signals of different protons on the DBC core are clearly observed at 7.79–8.90 ppm, and the proton signals of the side chain appear at 1.55, 1.90, and 4.70 ppm (Fig. S7). The ^{13}C NMR spectrum of Br-4PADBC shows the signals of different carbon atoms on the core from 113.10 to 137.06 ppm, along with those on the side chain between 20.78 and 42.51 ppm (Fig. S8). The ^{31}P NMR spectrum shows a single signal at 26.11 ppm corresponding to the only phosphorus atom in Br-4PADBC (Fig. S9). A dominant ionic peak at m/z = 560 observed at TOF-MS spectrum is consistent with the theoretical molecular weight of Br-4PADBC (Fig. S10).

Fig. 1(a and b) compares the molecular conformations of Br-4PADBC and MeO-2PACz optimized by density functional theory (DFT). Unlike the planar carbazole core within MeO-2PACz, the DBC core within Br-4PADBC exhibits a unique non-planar screw configuration with a dihedral angle of 13°. Along with the involvement of two electron-withdrawing Br atoms, this leads to increased dipole moment from 0.2 D (MeO-2PACz) to 6.1 D (Br-4PADBC), and this expects to increase the work function of the ITO substrate toward better matching with the highest occupied molecular orbital (HOMO) energy level of perovskite [31]. According to a comparison of the calculated electrostatic surface potential (ESP), there are obvious negative electrostatic potential surrounding on the Br atoms (Fig. 1a).

Moreover, owing to the involvement of the electron-withdrawing Br atoms, the HOMO energy level of Br-4PADBC (−5.72 eV) is much deeper than that of MeO-2PACz (−5.24 eV). This result is consistent with the obvious positive shift of the oxidation potential of Br-4PADBC relative to MeO-2PACz measured by cyclic voltammetry (Fig. S11). Similar tendency is observed for their calculated lowest unoccupied molecular orbital (LUMO) energy levels (Fig. S12). As a result, the HOMO-LUMO gaps of both Br-4PADBC and MeO-2PACz are quite large, ensuring negligible parasitic absorption in the visible region as confirmed by ultraviolet-visible (UV-vis) absorption spectroscopic study (Fig. S13). Besides, the decomposition temperature corresponding to a 5% weight loss of Br-4PADBC reaches 316 °C, which is much higher than that of MeO-2PACz (271 °C), confirming the excellent thermal stability of Br-4PADBC and thus its suitability as HSL for tolerable follow-up annealing treatment of the perovskite film (Fig. S14).

It has been reported that the carbazole-based SAM such as 2PACz may easily aggregate to form dimers and other oligomers, leading to inhomogeneity in HSL and compromised device performance [23,28]. We used the dimer model and simulated the π-π

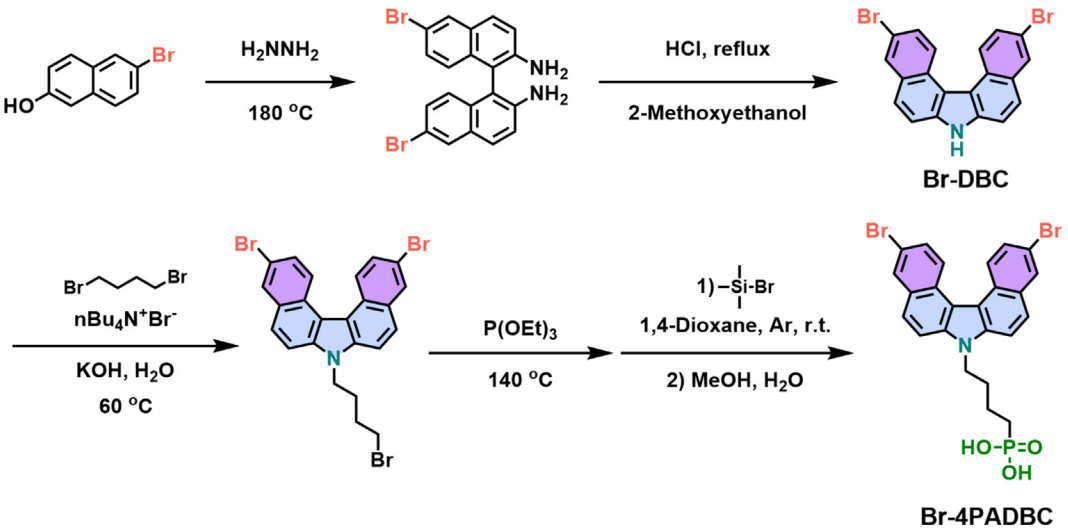

Scheme 1. Synthesis route of Br-4PADBC.

stacking of the Br-4PADBC and MeO-2PACz molecules by DFT. As shown in Fig. 1(c–e), both Br-4PADBC and MeO-2PACz exhibit quite large binding energy of −3.81 and −2.59 eV respectively along with relatively small stacking distances of ∼3.67 and ∼3.35 Å, suggesting their high tendency for aggregation. Upon mixing Br-4PADBC and MeO-2PACz to form bi-SAM, the binding energy dramatically decreases to −0.94 eV, along with the increase of the stacking distance to ∼3.92 Å. This suggests the inhibited tendency for aggregation for bi-SAM [15].

We then employed X-ray photoelectron spectroscopy (XPS) to confirm the successful anchoring of bi-SAM onto ITO substrate. Upon depositing either the individual Br-4PADBC/MeO-2PACz SAM or bi-SAM, prominent P signals are clearly detected in the P 2*p* XPS spectra (Fig. 1f), and Br signals appear in both Br-4PADBC and bi-SAM (Fig. 1g). These results confirm that Br-4PADBC and MeO-2PACz SAMs can be readily anchored onto ITO via the phosphate group [34]. Meanwhile, significant shifts towards higher binding energies of the In 3*d* and Sn 3*d* peaks of ITO with SAMs are observed (Fig. 1h and Fig. S15), indicating the robust interactions between SAMs and ITO substrate [35]. The shift of XPS binding energies is related to the dehydration condensation reaction between the P–OH bonds of SAM molecules phosphonic acid anchoring groups and In–OH or Sn–OH bonds on ITO surface during heating annealing, forming In–O–P and Sn–O–P covalent bonds. Indeed, theoretical calculations indicate the formation of covalent bonds between SAM with ITO (Fig. S16).

The electrical conductivity of HSL has a significant impact on hole transport and device performance [36–38]. We utilized conductive atomic force microscopy (c-AFM) to investigate the electrical conductivity difference of various SAMs. Fig. 2(a–c) compares the c-AFM images of MeO-2PACz, Br-4PADBC, and bi-SAM films deposited on ITO. MeO-2PACz exhibits an average current intensity of −0.818 pA, which is much larger than Br-4PADBC (−0.133 pA), indicating higher electrical conductivity of MeO-2PACz than Br-4PADBC. The lower electrical conductivity of Br-4PADBC is consistent with its inferior device efficiency as discussed below, and thus mixing it with MeO-2PACz to construct bi-SAM is necessary for high-efficiency device. For bi-SAM film, the average current intensity is −0.564 pA, which is much larger than that of Br-4PADBC, revealing its considerable electrical conductivity. We then examine the current distribution and find that mixing Br-4PADBC and MeO-2PACz leads to a more uniform distribution of current values (Fig. S17) [39]. On the other hand, the surface morphologies of different SAMs on ITO substrate are measured by atomic force microscopy (AFM). The root mean square (RMS) roughness values for MeO-2PACz, Br-4PADBC, and bi-SAM films deposited on ITO are determined to be 2.27, 2.52, and 2.03 nm respectively (Fig. S18). The bi-SAM film exhibits the smoothest surface, affording improved interfacial contact between SAM and perovskite layer [40].

Kelvin probe force microscopy (KPFM) was utilized to assess further the surface potential of SAM deposited on ITO substrate (Fig. 2d–f). As shown in Fig. 2(g), the contact potential difference (CPD) values for MeO-2PACz, Br-4PADBC, and bi-SAM film are −124, −208, and −156 mV respectively, indicating that both Br-4PADBC/ITO and bi-SAM/ITO possess higher work functions with deeper Fermi levels than MeO-2PACz/ITO [41]. Furthermore, high-resolution synchrotron radiation photoelectron spectroscopy (HR-SRPES) was employed to determine the energy levels of different SAMs and perovskite (Fig. S19). As illustrated in Fig. 2(h), due to the introduction of Br-4PADBC, the valence band (VB) energy level of bi-SAM/ITO (−5.51 eV) becomes closer to that of perovskite (−5.68 eV) than that of MeO-2PACz (−5.32 eV, see Table S1). This is anticipated to benefit enhancing the open-circuit voltage (V_{OC}) of device [42].

We next characterized the surface morphologies and crystallinities of perovskite films deposited on different SAMs. Fig. 3(a–c) compares the scanning electron microscopic (SEM) images of perovskite films on MeO-2PACz, Br-4PADBC, and bi-SAM. While all perovskite films look compact without discernible pinholes, the average grain sizes of perovskite on Br-4PADBC and bi-SAM are 656 and 658 nm respectively, which are much larger than that of MeO-2PACz/perovskite (439 nm, Fig. S20), revealing that Br-4PADBC helps to promote the crystallization of the atop perovskite film. Cross-sectional SEM analyses of perovskite films on different SAMs yield consistent results: perovskite films on Br-4PADBC and bi-SAM show much larger grains with less grain boundaries than that on MeO-2PACz (Fig. 3d–f). We compared the wettability of different SAMs through contact angle measurements (Fig. S21). The presence of Br-4PADBC leads to better wettability, which plays a significant role in reducing pinholes in perovskite films and improving the crystal size of perovskite films [13,43]. On the basis of a comparison of the AFM images of perovskite films on MeO-2PACz, Br-4PADBC, and bi-SAM, bi-SAM/perovskite film exhibits the smallest RMS roughness of 19.86 nm among the three films

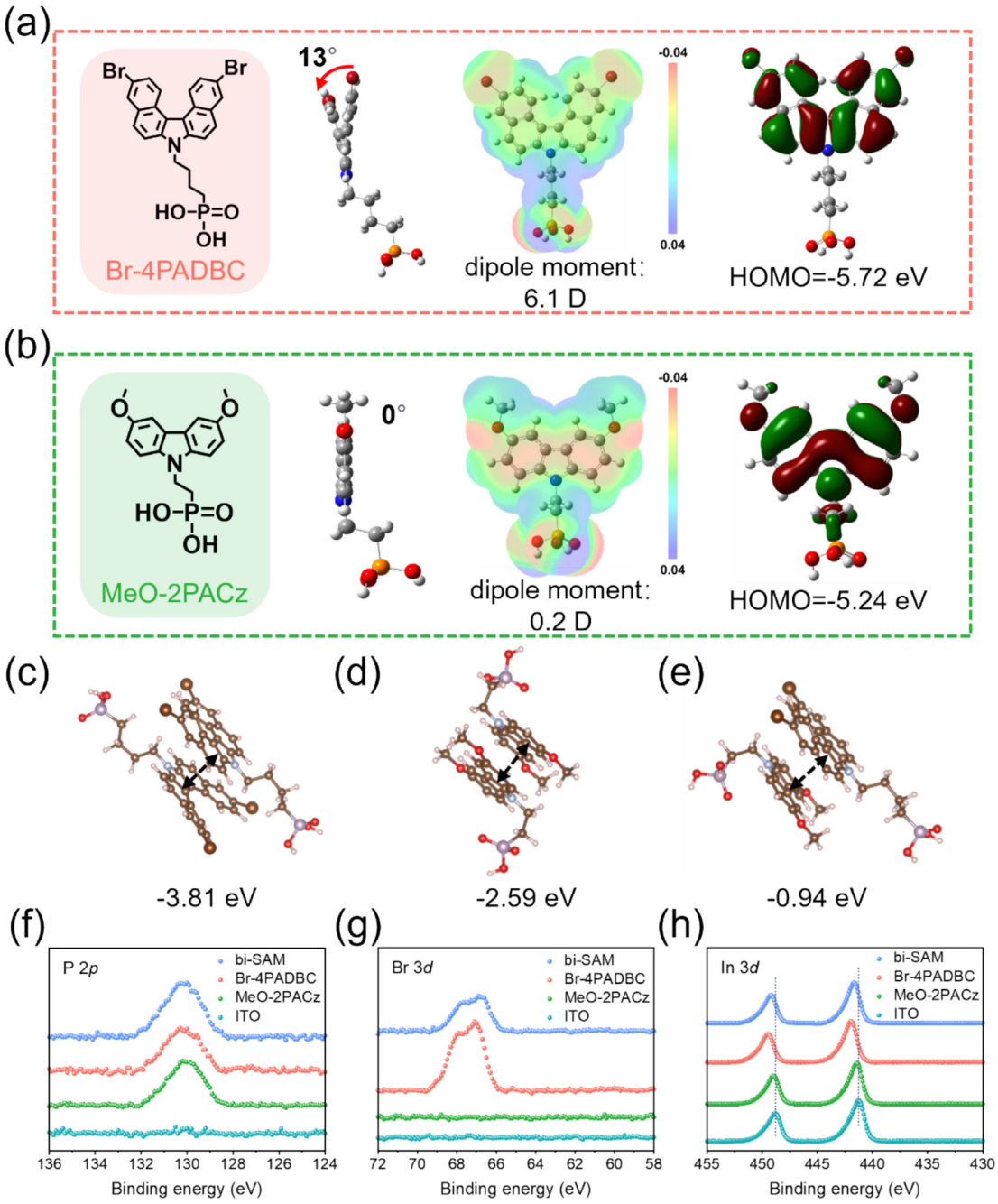

Fig. 1. The chemical structures, molecular conformations with dihedral angles, dipole moment, ESPs, and the HOMO energy levels of (a) Br-4PADBC and (b) MeO-2PACz. Calculation model of dimer of (c) Br-4PADBC, (d) MeO-2PACz, and (e) bi-SAM Br-4PADBC and MeO-2PACz. (f) P 2*p*, (g) Br 3*d*, and (h) In 3*d* XPS spectra of bare ITO, MeO-2PACz/ITO, Br-4PADBC/ITO, and bi-SAM/ITO.

(Fig. S22). This is inherited from the smoothest bi-SAM film as discussed above.

Grazing-incidence X-ray diffraction (GIXRD) was performed at an incidence angle of 0.5° to probe the impact of SAM on the crystallinity and crystal orientation of perovskite, in which the presence of a diffraction ring with a q value of 10 nm^{-1} corresponds to the (001) plane of perovskite [44]. As compared in Fig. 3(g–i), perovskite films on Br-4PADBC and bi-SAM both exhibit more pronounced and brighter (001) diffraction rings than that on MeO-2PACz/ITO, indicating improved crystallinity of perovskite films on Br-4PADBC and bi-SAM. Additionally, radial integrals derived from GIXRD patterns reveal stronger and sharper (001) diffraction peaks of perovskite films on Br-4PADBC and bi-SAM (Fig. S23), confirming improved crystallinity of perovskite films.

The presence of uncoordinated Pb^{2+} ions on the surface and at the grain boundaries of perovskite is the primary cause for trap state formation, thereby deteriorating carrier transport [45,46]. The interfacial interactions between the Br-4PADBC/MeO-2PACz SAM and the uncoordinated Pb^{2+} ions within perovskite are investigated by ^{1}H NMR spectroscopic analysis based on a simplified solution blend of SAM and PbI_2 dissolved in DMSO32-d_6 (Fig. S24). After blending with PbI_2, the proton signals of the aromatic rings in both Br-4PADBC and MeO-2PACz shift towards higher field, and Br-4PADBC exhibited a more pronounced shift

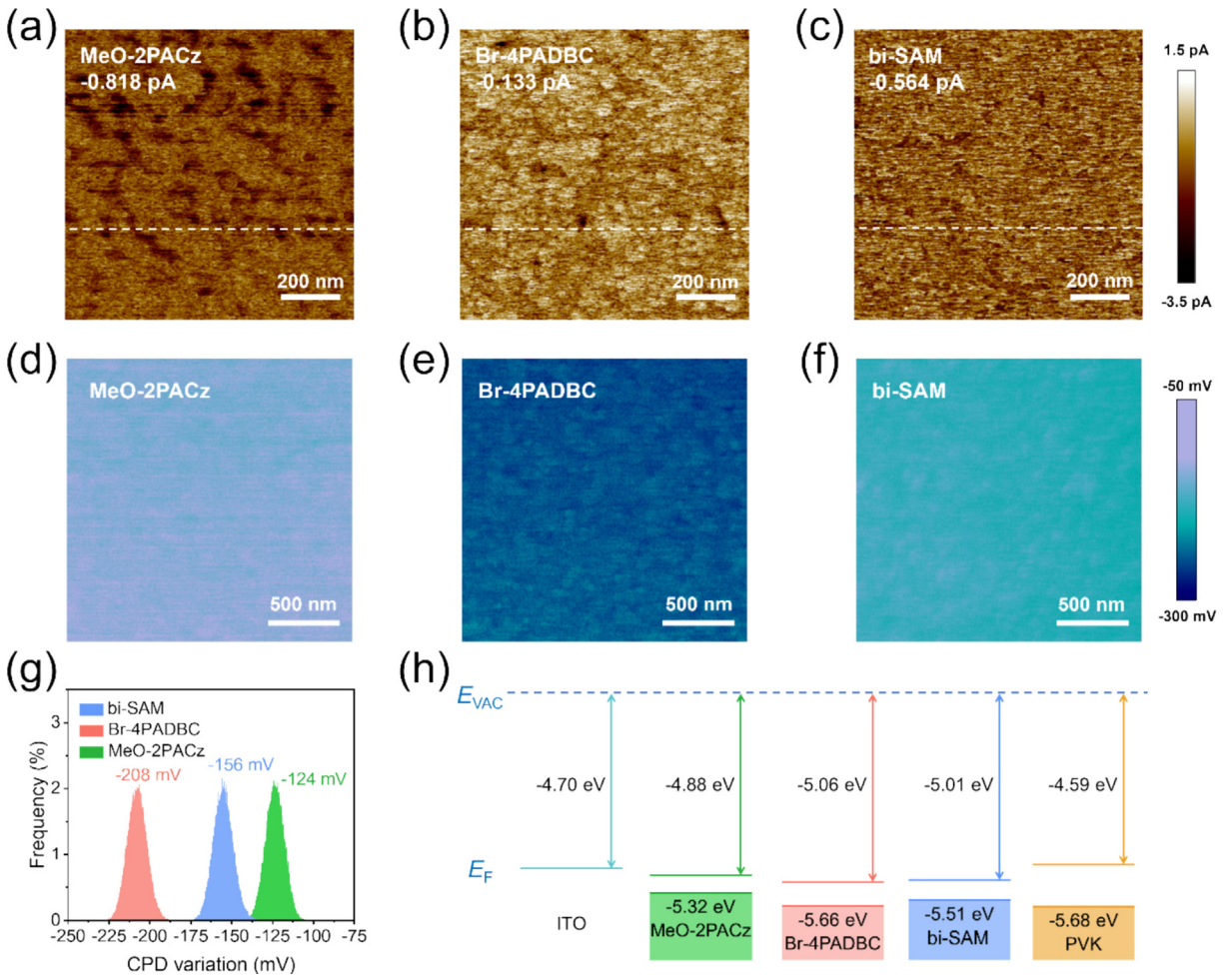

Fig. 2. C-afm images of (a) meo-2pacz/ito, (b) br-4padbc/ito, and (c) bi-sam/ito. surface potential distribution of (d) meo-2pacz, (e) br-4padbc, and (f) bi-SAM treated ITO. (g) Surface contact potential difference. (h) Diagram of energy-level alignments.

in the proton peak, indicating stronger coordination interactions between Br atoms and Pb^{2+} ions [14]. This result suggests reinforced coordination interactions between Br atoms within Br-4PADBC and uncoordinated Pb^{2+} ions, leading to improved crystallization of perovskite film as discussed above.

We then fabricated the inverted PSC devices using SAM as HSL with an architecture of ITO/SAM/perovskite/C_{60}/BCP/Ag (Fig. 4a) so as to assess the dependence of device photovoltaic performance on SAM. The current-voltage (*J-V*) characteristics of the best-performing devices with different SAMs measured under standard air mass 1.5 global (AM 1.5 G) conditions are compared in Fig. 4(b), and the corresponding device parameters are summarized in Table S2. The proportion optimization of bi-SAM can be found in Fig. S25 and Table S3. The control single-component MeO-2PACz device exhibits a PCE of 23.91%, with a V_{OC}, a short circuit current (J_{SC}), and a fill factor (FF) of 1.137 V, 25.49 mA cm^{-2}, and 82.52%, respectively. Upon using single-component Br-4PADBC SAM, the PCE is 20.61% calculated from V_{OC}, J_{SC}, and FF values of 1.164 V, 24.87 mA cm^{-2}, and 71.19%, respectively. The bi-SAM-based target device attains a higher PCE of 24.52% than the control MeO-2PACz one, with the corresponding V_{OC}, J_{SC}, and FF values reaching 1.163 V, 25.50 mA cm^{-2}, and 82.82% (Fig. 4c). Hence, bi-SAM affords improved PCE relative to the single-component MeO-2PACz/Br-4PADBC SAM. The considerable reproducibility of devices was verified by the statistical photovoltaic parameters based on 30 independent devices (Fig. S26), from which clearly the PCE enhancement of the bi-SAM device is primarily attributed to the increase of V_{OC}. On the other hand, J_{SC} of the bi-SAM device exhibits negligible change relative to the control MeO-2PACz device, as verified by external quantum efficiency (EQE) measurements (Fig. 4d and Fig. S27).

The stabilized power output (SPO) of the bi-SAM device is consistently monitored at the maximum power point (V_{max}, 1.01 V) under continuous one sun illumination, exhibiting a SPO of 24.11% within 250 s (Fig. 4e). We further investigated the influence of SAM HSL on the thermal and operational stabilities of devices. The thermal stability of unencapsulated devices was recorded at 85 °C in a N_2 glovebox. After 800 h continuous heating, thanks to the excellent thermal stability of Br-4PADBC device, the bi-SAM device retains ~90% of its initial PCE, which is dramatically higher than the control MeO-2PACz device with only ~76% PCE retained (Fig. 4f). Moreover, the operational stability of the unencapsulated device was also tracked under light-emitting diode (LED) illumination (100 mW cm^{-2}) for 1000 h at maximum power point (MPP) in a N_2 glovebox. As illustrated in Fig. 4(g), the bi-SAM device maintains ~82% of its initial PCE after 1000 h continuous illumination. Such durability is comparable to that of the Br-4PADBC device but much higher than that of the control MeO-2PACz device (~63%). These results indicate that the incorporation of Br-4PADBC in bi-SAM improves the thermal and operational stabilities of devices in addition to the increased PCE. The improvement in stability is attributed to stronger interactions between

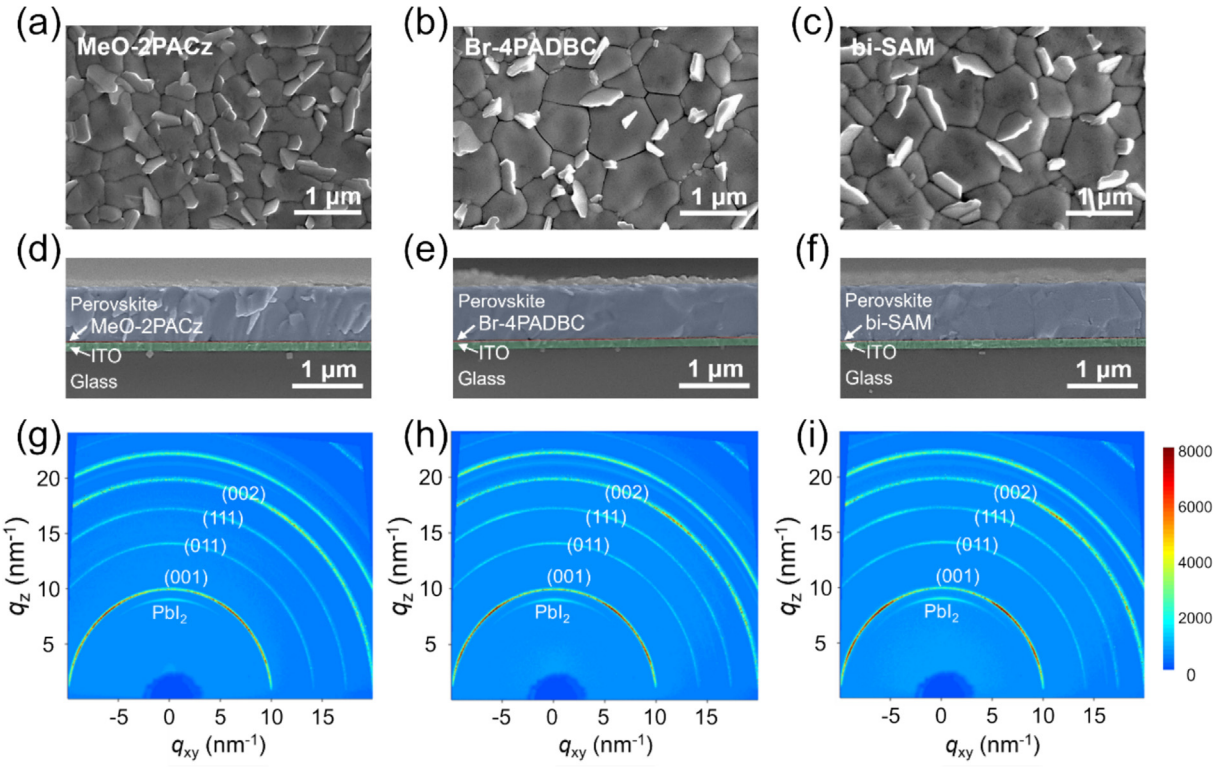

Fig. 3. Top-view SEM images of perovskite films deposited on (a) MeO-2PACz/ITO, (b) Br-4PADBC/ITO, and (c) bi-SAM/ITO substrates. Cross-section SEM image of the perovskite films deposited on (d) MeO-2PACz/ITO, (e) Br-4PADBC/ITO, and (f) bi-SAM/ITO. Two-dimensional GIXRD patterns of perovskite films deposited on (g) MeO-2PACz/ITO, (h) Br-4PADBC/ITO, and (i) bi-SAM/ITO.

Br-4PADBC and perovskite, as well as the enhanced wettability. As a result, the perovskite crystal size is significantly increased, enabling improved stability under prolonged high temperature or light exposure conditions.

We further investigated the interfacial carrier dynamics using femtosecond transient absorption spectroscopy (TAS). Two-dimensional color images of TAS spectra acquired from perovskite side deposited on ITO/SAM are illustrated in Fig. 5(a–c). The formation of a ground state bleaching (GSB) peak at 770 nm is observed for all samples, and subsequent quenching of the GSB peak is detected within the time ranging from 5 to 2000 ps. The quenching rate of the GSB peak corresponds to the hole transport efficiency from perovskite to HSL [47–49]. Bi-SAM/perovskite shows the largest quenching of the GSB peak within a time frame of 2000 ps, suggesting its highest efficiency of hole extraction at the SAM/perovskite interface (Fig. S28) [50]. According to the fitting results of the decay kinetic curve of TAS spectra, the fitted decay lifetimes of perovskite films on MeO-2PACz, Br-4PADBC, and bi-SAM are 1427, 2061, and 1273 ps respectively (Fig. S29 and Table S4). The smallest decay lifetime of bi-SAM/perovskite film confirms the facilitated hole extraction at the bi-SAM/perovskite interface.

To understand the mechanism responsible for the increase of V_{OC}, we carried out several characterizations to unveil the effect of SAM on the charge carrier dynamics of the device. Steady-state photoluminescence (PL) and time-resolved photoluminescence (TRPL) spectra of perovskite films deposited on different SAMs are measured to further evaluate the nonradiative recombination. The bi-SAM exhibits the lowest PL intensity (Fig. 5d), suggesting its largest hole extraction capability [31]. According to TRPL attenuation results, the carrier lifetime of perovskite on bi-SAM is 608.88 ns, smaller than that of perovskite films on MeO-2PACz (635.94 ns) and Br-4PADBC (1021.85 ns) (Fig. 5(e) and Table S5). This result confirms the most efficient hole extraction achieved by the bi-SAM [14,41]. Furthermore, the Urbach energy (E_u) can be determined from UV-Vis absorption spectrum as a mean to assess the perovskite film quality [51]. The perovskite film deposited on bi-SAM exhibits a smaller E_u (40.71 meV) than that on MeO-2PACz (46.84 meV, Fig. 5f) due to the incorporation of Br-4PADBC, suggesting that Br-4PADBC induces the enhanced film quality of perovskite [22]. We also carried out photoluminescence quantum yield (PLQY) measurements to probe the nonradiative recombination within the perovskite films, from which the internal electron-hole quasi-Fermi level splitting (QFLS) can be calculated by the equation: QFLS = $k_BT \times \ln(\text{PLQY} \times J_G/J_{0,rad})$, where k_B and T represent Boltzmann constant and temperature, respectively; J_G is the current density under illumination; and $J_{0,rad}$ is the dark radiative recombination saturation current density [52,53]. The PLQY values of the perovskite films deposited on MeO-2PACz, Br-4PADBC, and bi-SAM are 1.59%, 2.13%, and 2.09%, corresponding to QFLS values of 1.173, 1.181, and 1.180 eV, respectively (Fig. 5g). The increases of QFLS value for Br-4PADBC and bi-SAM suggests the effective passivation of perovskite defects, resulting in the inhibited non-radiative recombination at the SAM/perovskite interface and consequently the increase of V_{OC}.

The transient photocurrent/photovoltage (TPC/TPV) techniques are employed to investigate the charge extraction lifetime and recombination lifetime in devices [43]. The TPC curve indicates that bi-SAM device exhibits the smallest charge extraction lifetime of 0.39 μs (Fig. 5h), revealing the accelerated interfacial charge extraction. Besides, the largest charge recombination lifetime of 5.26 μs is obtained for bi-SAM device in the TPV curve (Fig. S30), further confirming the reduced non-radiative recombination [54]. To evaluate the trap density, we implemented space charge limited current (SCLC) test via a configuration of ITO/SAM/Perovskite/Spiro-OMeTAD/Ag. The turning points at the ohmic and trap regions of the curves reveal the trap-filled limit voltage (V_{TFL}) values, which are demonstrated to be 0.712 V for MeO-2PACz, 0.625 V for Br-4PADBC, and 0.601 V for bi-SAM, respectively (Fig. S31). The trap

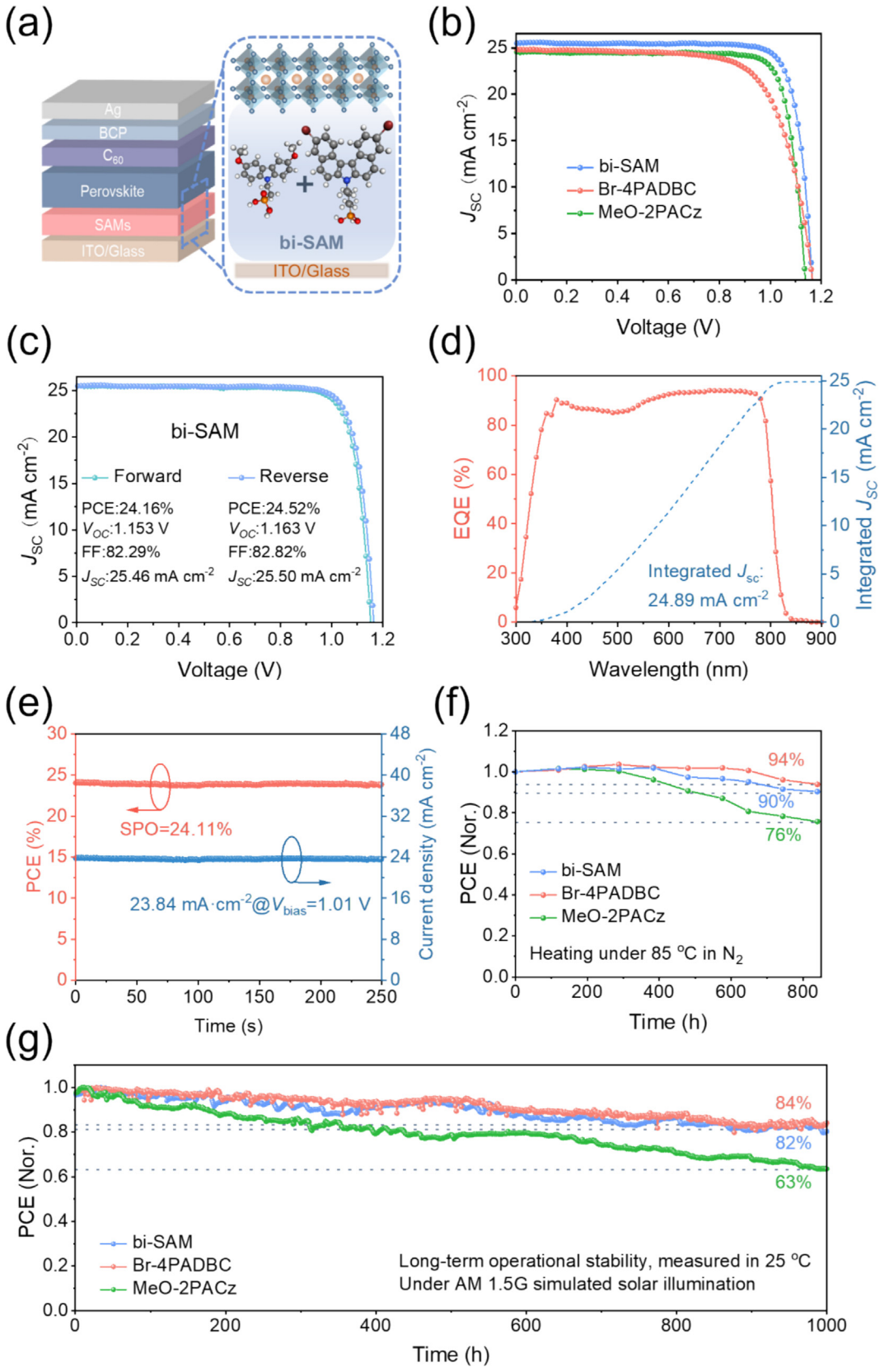

Fig. 4. (a) Device structure of inverted PSCs based on bi-SAM HSL. (b) Current density-voltage (*J-V*) characteristics of devices based on different HSLs. (c) *J-V* curves of the best-performing bi-SAM devices. (d) EQE spectra and corresponding integrated photocurrents of PSCs based on bi-SAM. (e) The stabilized power output at the maximum power point for bi-SAM based champion devices. (f) Normalized PCE of PSCs deposited on three types of HSLs in an 85 °C N_2 glove box. (g) Maximum power point tracking for 1000 h of three types of HSLs devices under continuous 1 sun illumination in N_2 atmosphere.

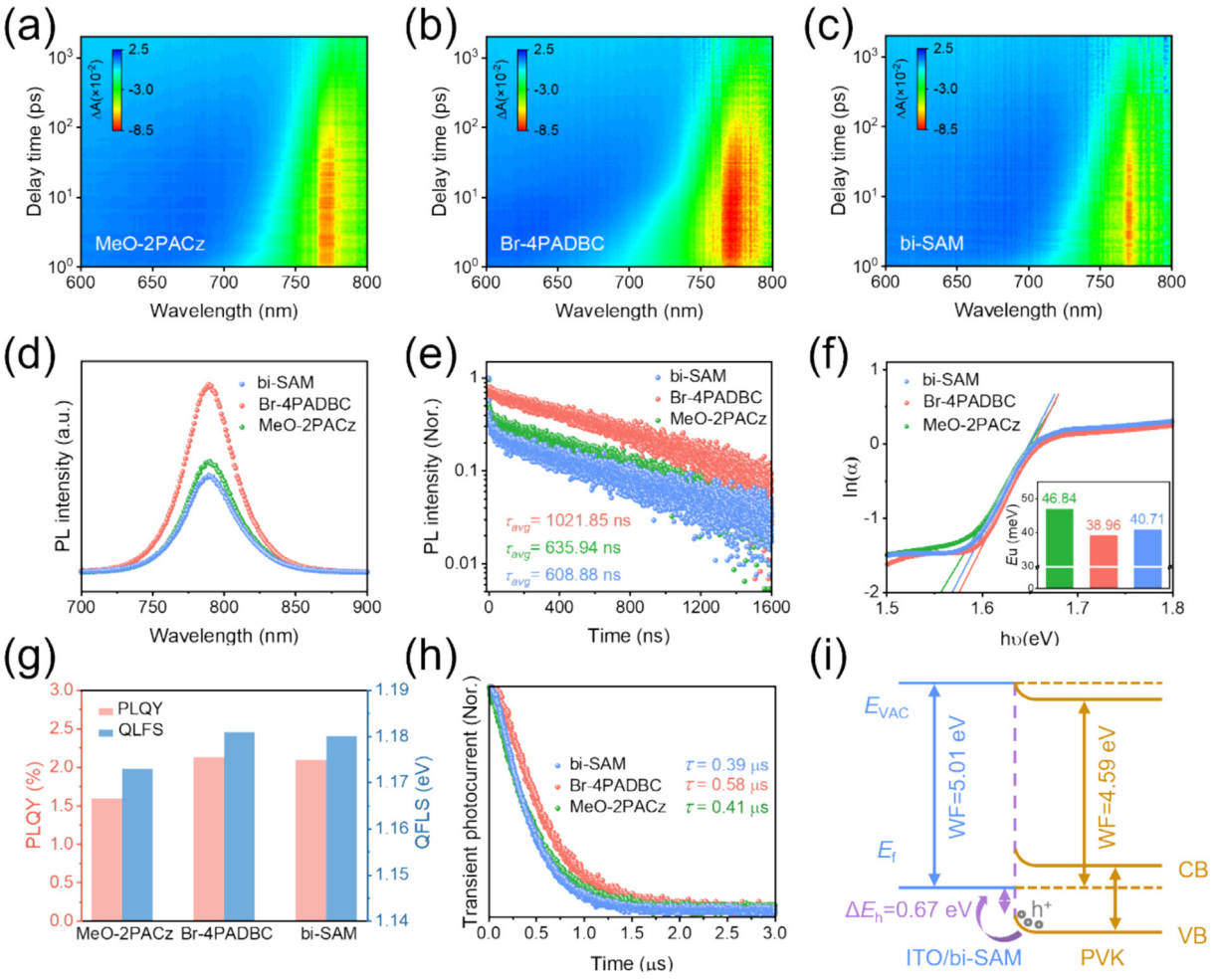

Fig. 5. TAS of perovskite films deposited on (a) MeO-2PACz/ITO, (b) Br-4PADBC/ITO, and (c) bi-SAM/ITO. (d) Steady-state PL spectra and (e) TRPL decay curves of perovskite films deposited on three HSLs. (f) Logarithm of absorption coefficient versus photon energy and Urbach energy (inset) calculated in perovskites consisting of ITO/HSLs/perovskite. (g) PLQY and QFLS of perovskites deposited on three HSLs. (h) TPC attenuation of PSCs prepared with different HSLs. (i) Interfacial energy level diagram of contact between bi-SAM/ITO and perovskite.

densities (N_{trap}) for the Br-4PADBC and bi-SAM based devices were calculated to be 5.76 × 10^{15} and 5.54 × 10^{15} cm^{-3}, respectively, which are lower than that of the MeO-2PACz based device (6.57 × 10^{15} cm^{-3}), which confirm the decrease in trap density [55].

Finally, the energy level alignment between SAM and perovskite is examined to unveil the factor from energy level aspect beneficial for the increase of V_{OC}. As discussed above, after the modification of MeO-2PACz, Br-4PADBC, and bi-SAM, the work function (WF) of ITO increases from 4.70 to 4.88, 5.06, and 5.01 eV, respectively (Fig. 5i and Fig. S32). The contact between the bare ITO and perovskite induces a slight upwards band bending, resulting in a large barrier for hole extraction (ΔE_h) of 0.98 eV. After modification by MeO-2PACz, Br-4PADBC, and bi-SAM, the ΔE_h value decreases to 0.80, 0.62, and 0.67 eV respectively. Hence, the incorporation of Br-4PADBC within bi-SAM leads to a decrease of ΔE_h value to 0.67 eV, benefiting hole extraction at the ITO/perovskite interface [15,56].

3. Conclusions

In summary, we synthesize a novel SAM molecule Br-4PADBC bearing a non-planar DBC core grafting two Br atoms. The involvement of the non-planar Br-DBC terminal group enables a much larger dipole moment of Br-4PADBC than the commonly used MeO-2PACz SAM, leading to much deeper work function of ITO with better alignment with the VB energy level of perovskite. Additionally, the introduction of Br atoms improves the quality of perovskite crystals and effectively passivates the defects in perovskite. We then develop a bi-SAM strategy by applying Br-4PADBC as a second component to the MeO-2PACz SAM, accomplishing complementary hole transport in inverted PSCs and consequently enhanced PCE from 23.91% to 24.52%. The enhanced PCE of bi-SAM device is attributed primarily to the increase of V_{OC}, which stems from effective passivation of perovskite defects, inhibited non-radiative recombination, and increased work function of ITO rendering decrease of the energy level barrier between ITO and perovskite. The bi-SAM strategy further enables dramatic improvements of both thermal and operational stabilities of the PSC devices. Our bi-SAM strategy with complementary functions of distinct SAMs paves the way for efficiency enhancement of PSCs towards commercialization.

Experimental section

Experimental details can be found in the Supporting Information.

CRediT authorship contribution statement

Shantao Zhang: Writing – original draft, Investigation, Formal analysis, Data curation, Conceptualization. **Xiaofen Jiang:** Writing – original draft, Formal analysis, Data curation, Conceptualization. **Xue Wang:** Data curation, Conceptualization. **Yan Gao:** Data curation. **TianAo Hou:** Data curation. **Xiaoqian Teng:** Data curation. **Haolin Wang:** Data curation. **Wenjing Chen:** Data curation. **Shuang Gao:** Data curation. **Xinyu Li:** Data curation. **Ziqi Hu:** Writing – original draft, Investigation, Formal analysis, Data curation. **Xiaojun Wu:** Data curation. **Zhengguo Xiao:** Data curation. **Tao Chen:** Data curation. **Yanwu Zhu:** Data curation. **Yalin Lu:** Data curation. **Xiaocheng Zeng:** Data curation. **Zonglong Zhu:** Writing – review & editing, Writing – original draft, Formal analysis, Data curation, Conceptualization. **Shangfeng Yang:** Writing – review & editing, Writing – original draft, Investigation, Funding acquisition, Formal analysis, Data curation, Conceptualization.

Declaration of competing interest

The authors declare that they have no known competing financial interests or personal relationships that could have appeared to influence the work reported in this paper.

Acknowledgments

S.Z., X.J., X.W. and Y.G. contributed equally to this work. S.Y. acknowledges the National Natural Science Foundation of China (51925206, U1932214, 52302052), the Strategic Priority Research Program of the Chinese Academy of Sciences (XDB0450301), the Fundamental Research Funds for the Central Universities (WK2060000051, 20720220009). Z. Z. acknowledges the National Key Research and Development Program of China (No. 2023YFB3809700), the Innovation and Technology Fund (GHP/100/20SZ, GHP/102/20GD, MRP/040/21X, ITS/147/22FP), the Research Grants Council of Hong Kong Grant (N_CityU102/23, C4005-22Y, C1055-23G, 11306521), the Green Tech Fund (GTF202020164), the Science Technology and Innovation Committee of Shenzhen Municipality (SGDX20210823104002015, JCYJ20220818101018038), the National Natural Science Foundation of China (52322318). This work was partially carried out at the Instruments Center for Physical Science, University of Science and Technology of China. We thank the beamlines BL14B1 at Shanghai Synchrotron Radiation Facility (SSRF) and BL11U at National Synchrotron Radiation Laboratory (NSRL) for providing the beam time.

Appendix A. Supplementary material

Supplementary data to this article can be found online at https://doi.org/10.1016/j.jechem.2024.12.040.

References

[1] H. Min, D.Y. Lee, J. Kim, G. Kim, K.S. Lee, J. Kim, M.J. Paik, Y.K. Kim, K.S. Kim, M. G. Kim, T.J. Shin, S. Il Seok, Nature 598 (2021) 444–450.
[2] X. Wu, B. Li, Z. Zhu, C.-C. Chueh, A.K.Y. Jen, Chem. Soc. Rev. 50 (2021) 13090–13128.
[3] Z. Li, X. Wu, B. Li, S. Zhang, D. Gao, Y. Liu, X. Li, N. Zhang, X. Hu, C. Zhi, A.K.Y. Jen, Z. Zhu, Adv. Energy Mater. 12 (2021) 2103236.
[4] W. Peng, K. Mao, F. Cai, H. Meng, Z. Zhu, T. Li, S. Yuan, Z. Xu, X. Feng, J. Xu, M.D. McGehee, J. Xu, Science 379 (2023) 683–690.
[5] Z. Huang, Y. Bai, X. Huang, J. Li, Y. Wu, Y. Chen, K. Li, X. Niu, N. Li, G. Liu, Y. Zhang, H. Zai, Q. Chen, T. Lei, L. Wang, H. Zhou, Nature 623 (2023) 531–537.
[6] X. Li, X. Wu, B. Li, Z. Cen, Y. Shang, W. Lian, R. Cao, L. Jia, Z. Li, D. Gao, X. Jiang, T. Chen, Y. Lu, Z. Zhu, S. Yang, Energy Environ. Sci. 15 (2022) 4813–4822.
[7] Z. Li, B. Li, X. Wu, S.A. Sheppard, S. Zhang, D. Gao, N.J. Long, Z. Zhu, Science 376 (2022) 416–420.
[8] Z. Liang, Y. Zhang, H. Xu, W. Chen, B. Liu, J. Zhang, H. Zhang, Z. Wang, D.-H. Kang, J. Zeng, X. Gao, Q. Wang, H. Hu, H. Zhou, X. Cai, X. Tian, P. Reiss, B. Xu, T. Kirchartz, Z. Xiao, S. Dai, N.-G. Park, J. Ye, X. Pan, Nature 624 (2023) 557–563.
[9] X. Li, W. Zhang, X. Guo, C. Lu, J. Wei, J. Fang, Science 375 (2022) 434–437.
[10] D. Gao, B. Li, Z. Li, X. Wu, S. Zhang, D. Zhao, X. Jiang, C. Zhang, Y. Wang, Z. Li, N. Li, S. Xiao, W.C.H. Choy, A.K.Y. Jen, S. Yang, Z. Zhu, Adv. Mater. 35 (2022) 2206387.
[11] M. Li, M. Liu, F. Qi, F.R. Lin, A.K.Y. Jen, Chem. Rev. 124 (2024) 2138–2204.
[12] Y. Duan, Y. Chen, Y. Wu, Z. Liu, S. Liu, Q. Peng, Adv. Funct. Mater. 34 (2024) 2315604.
[13] S. Zhang, F. Ye, X. Wang, R. Chen, H. Zhang, L. Zhan, X. Jiang, Y. Li, X. Ji, S. Liu, M. Yu, F. Yu, Y. Zhang, R. Wu, Z. Liu, Z. Ning, D. Neher, L. Han, Y. Lin, H. Tian, W. Chen, M. Stolterfoht, L. Zhang, W.-H. Zhu, Y. Wu, Science 380 (2023) 404–409.
[14] Z. Li, X. Sun, X. Zheng, B. Li, D. Gao, S. Zhang, X. Wu, S. Li, J. Gong, J.M. Luther, Z. a. Li, Z. Zhu, Science 382 (2023) 284–289.
[15] Q. Tan, Z. Li, G. Luo, X. Zhang, B. Che, G. Chen, H. Gao, D. He, G. Ma, J. Wang, J. Xiu, H. Yi, T. Chen, Z. He, Nature 620 (2023) 545–551.
[16] R. He, W. Wang, Z. Yi, F. Lang, C. Chen, J. Luo, J. Zhu, J. Thiesbrummel, S. Shah, K. Wei, Y. Luo, C. Wang, H. Lai, H. Huang, J. Zhou, B. Zou, X. Yin, S. Ren, X. Hao, L. Wu, J. Zhang, J. Zhang, M. Stolterfoht, F. Fu, W. Tang, D. Zhao, Nature 618 (2023) 80–86.
[17] Q. Cao, T. Wang, X. Pu, X. He, M. Xiao, H. Chen, L. Zhuang, Q. Wei, H.-L. Loi, P. Guo, B. Kang, G. Feng, J. Zhuang, G. Feng, X. Li, F. Yan, Adv. Mater. 36 (2024) 2311970.
[18] P.J. Hotchkiss, S.C. Jones, S.A. Paniagua, A. Sharma, B. Kippelen, N.R. Armstrong, S.R. Marder, Acc. Chem. Res. 45 (2012) 337–346.
[19] S.Y. Kim, S.J. Cho, S.E. Byeon, X. He, H.J. Yoon, Adv. Energy Mater. 10 (2020) 2002606.
[20] S. Zhang, R. Wu, C. Mu, Y. Wang, L. Han, Y. Wu, W.-H. Zhu, ACS Mater. Lett. 4 (2022) 1976–1983.
[21] M. Liu, M. Li, Y. Li, Y. An, Z. Yao, B. Fan, F. Qi, K. Liu, H.L. Yip, F.R. Lin, A.K.Y. Jen, Adv. Energy Mater. 14 (2024) 2303742.
[22] H. Bi, Y. Fujiwara, G. Kapil, D. Tavgeniene, Z. Zhang, L. Wang, C. Ding, S.R. Sahamir, A.K. Baranwal, Y. Sanehira, K. Takeshi, G. Shi, T. Bessho, H. Segawa, S. Grigalevicius, Q. Shen, S. Hayase, Adv. Funct. Mater. 33 (2023) 2300089.
[23] M. Liu, L. Bi, W. Jiang, Z. Zeng, S.-W. Tsang, F.R. Lin, A.-K.-Y. Jen, Adv. Mater. 35 (2023) 2304415.
[24] A. Magomedov, A. Al-Ashouri, E. Kasparavičius, S. Strazdaite, G. Niaura, M. Jošt, T. Malinauskas, S. Albrecht, V. Getautis, Adv. Energy Mater. 8 (2018) 1801892.
[25] E. Li, E. Bi, Y. Wu, W. Zhang, L. Li, H. Chen, L. Han, H. Tian, W.-H. Zhu, Adv. Funct. Mater. 30 (2020) 1909509.
[26] L. Li, Y. Wang, X. Wang, R. Lin, X. Luo, Z. Liu, K. Zhou, S. Xiong, Q. Bao, G. Chen, Y. Tian, Y. Deng, K. Xiao, J. Wu, M.I. Saidaminov, H. Lin, C.-Q. Ma, Z. Zhao, Y. Wu, L. Zhang, H. Tan, Nat. Energy 7 (2022) 708–717.
[27] X. Deng, F. Qi, F. Li, S. Wu, F.R. Lin, Z. Zhang, Z. Guan, Z. Yang, C.-S. Lee, A.-K.-Y. Jen, Angew. Chem. Int. Ed. 61 (2022) e202203088.
[28] S.M. Park, M. Wei, N. Lempesis, W. Yu, T. Hossain, L. Agosta, V. Carnevali, H.R. Atapattu, P. Serles, F.T. Eickemeyer, H. Shin, M. Vafaie, D. Choi, K. Darabi, E.D. Jung, Y. Yang, D.B. Kim, S.M. Zakeeruddin, B. Chen, A. Amassian, T. Filleter, M.G. Kanatzidis, K.R. Graham, L. Xiao, U. Rothlisberger, M. Grätzel, E.H. Sargent, Nature 624 (2023) 289–294.
[29] Q. Jiang, R. Tirawat, R.A. Kerner, E.A. Gaulding, Y. Xian, X. Wang, J.M. Newkirk, Y. Yan, J.J. Berry, K. Zhu, Nature 623 (2023) 313–318.
[30] A. Al-Ashouri, M. Marčinskas, E. Kasparavičius, T. Malinauskas, A. Palmstrom, V. Getautis, S. Albrecht, M.D. McGehee, A. Magomedov, ACS Energy Lett. 8 (2023) 898–900.
[31] W. Jiang, F. Li, M. Li, F. Qi, F.R. Lin, A.-K.-Y. Jen, Angew. Chem. Int. Ed. 61 (2022) e202213560.
[32] Z. Yi, W. Wang, R. He, J. Zhu, W. Jiao, Y. Luo, Y. Xu, Y. Wang, Z. Zeng, K. Wei, J. Zhang, S.-W. Tsang, C. Chen, W. Tang, D. Zhao, Energy Environ. Sci. 17 (2024) 202–209.
[33] Z. Li, Q. Tan, G. Chen, H. Gao, J. Wang, X. Zhang, J. Xiu, W. Chen, Z. He, Nanoscale 15 (2023) 1676–1686.
[34] W. Wang, Z. Lin, S. Gao, W. Zhu, X. Song, W. Tang, Adv. Funct. Mater. 33 (2023) 2303653.
[35] A. Asyuda, M. Gärtner, X. Wan, I. Burkhart, T. Saßmannshausen, A. Terfort, M. Zharnikov, J. Phys. Chem. C 124 (2020) 8775–8785.
[36] S. Yu, Z. Xiong, H. Zhou, Q. Zhang, Z. Wang, F. Ma, Z. Qu, Y. Zhao, X. Chu, X. Zhang, J. You, Science 382 (2023) 1399–1404.
[37] F. Ye, S. Zhang, J. Warby, J. Wu, E. Gutierrez-Partida, F. Lang, S. Shah, E. Saglamkaya, B. Sun, F. Zu, S. Shoaee, H. Wang, B. Stiller, D. Neher, W.-H. Zhu, M. Stolterfoht, Y. Wu, Nat. Commun. 13 (2022) 7454.
[38] N. Phung, M. Verheijen, A. Todinova, K. Datta, M. Verhage, A. Al-Ashouri, H. Köbler, X. Li, A. Abate, S. Albrecht, M. Creatore, ACS Appl. Mater. Interfaces 14 (2021) 2166–2176.
[39] Z. Ren, Z. Cui, X. Shi, L. Wang, Y. Dou, F. Wang, H. Lin, H. Yan, S. Chen, Joule 7 (2023) 2894–2904.
[40] S.N. Afraj, C.-H. Kuan, J.-S. Lin, J.-S. Ni, A. Velusamy, M.-C. Chen, E.-W.-G. Diau, Adv. Funct. Mater. 33 (2023) 2213939.
[41] C. Li, Z. Zhang, H. Zhang, W. Yan, Y. Li, L. Liang, W. Yu, X. Yu, Y. Wang, Y. Yang, M.K. Nazeeruddin, P. Gao, Angew. Chem. Int. Ed. 63 (2024) e202315281.
[42] M. Stolterfoht, P. Caprioglio, C.M. Wolff, J.A. Márquez, J. Nordmann, S. Zhang, D. Rothhardt, U. Hörmann, Y. Amir, A. Redinger, L. Kegelmann, F. Zu, S. Albrecht, N. Koch, T. Kirchartz, M. Saliba, T. Unold, D. Neher, Energy Environ. Sci. 12 (2019) 2778–2788.

[43] H. Zhang, S. Zhang, X. Ji, J. He, H. Guo, S. Wang, W. Wu, W.H. Zhu, Y. Wu, Angew. Chem. Int. Ed. 63 (2024) e202401260.
[44] X. Jiang, B. Liu, X. Wu, S. Zhang, D. Zhang, X. Wang, S. Gao, Z. Huang, H. Wang, B. Li, Z. Xiao, T. Chen, A.-K.-Y. Jen, S. Xiao, S. Yang, Z. Zhu, Adv. Mater. 36 (2024) 2313524.
[45] F. Gao, Y. Zhao, X. Zhang, J. You, Adv. Energy Mater. 10 (2019) 1902650.
[46] L.K. Ono, S. Liu, Y. Qi, Angew. Chem. Int. Ed. 59 (2020) 6676–6698.
[47] C.-M. Hung, C.-L. Mai, C.-C. Wu, B.-H. Chen, C.-H. Lu, C.-C. Chu, M.-C. Wang, S.-D. Yang, H.-C. Chen, C.-Y. Yeh, P.-T. Chou, Angew. Chem. Int. Ed. 62 (2023) e202309831.
[48] T.J. Miao, J. Tang, J. Chem. Phys. 152 (2020) 194201.
[49] J. Liu, J. Chen, P. Xu, L. Xie, S. Yang, Y. Meng, M. Li, C. Xiao, M. Yang, Z. Ge, Adv. Energy Mater. 14 (2024) 2303092.
[50] T. Wu, X. Xu, L.K. Ono, T. Guo, S. Mariotti, C. Ding, S. Yuan, C. Zhang, J. Zhang, K. Mitrofanov, Q. Zhang, S. Raj, X. Liu, H. Segawa, P. Ji, T. Li, R. Kabe, L. Han, A. Narita, Y. Qi, Adv. Mater. 35 (2023) 2300169.
[51] G. Kim, H. Min, K.S. Lee, D.Y. Lee, S.M. Yoon, S.I. Seok, Science 370 (2020) 108–112.
[52] I.L. Braly, H.W. Hillhouse, J. Phys. Chem. C 120 (2016) 893–902.
[53] P. Caprioglio, M. Stolterfoht, C.M. Wolff, T. Unold, B. Rech, S. Albrecht, D. Neher, Adv. Energy Mater. 9 (2019) 1901631.
[54] R. Guo, X. Zhang, X. Zheng, L. Li, M. Li, Y. Zhao, S. Zhang, L. Luo, S. You, W. Li, Z. Gong, R. Huang, Y. Cui, Y. Rong, H. Zeng, X. Li, Adv. Funct. Mater. 33 (2023) 2211955.
[55] X. Li, S. Gao, X. Wu, Q. Liu, L. Zhu, C. Wang, Y. Wang, Z. Liu, W. Chen, X. Li, P. Xiao, Q. Huang, T. Chen, Z. Li, X. Gao, Z. Xiao, Y. Lu, X. Zeng, S. Xiao, Z. Zhu, S. Yang, Joule 8 (2024) 3169–3185.
[56] W. Chen, Y. Zhou, L. Wang, Y. Wu, B. Tu, B. Yu, F. Liu, H.W. Tam, G. Wang, A.B. Djurišić, L. Huang, Z. He, Adv. Mater. 30 (2018) 1800515.